SUSCEPTIBILITY-BASED TIME-RESOLVED WHOLE-ORGAN AND REGIONAL TISSUE OXIMETRY

Felix W Wehrli[1], **Audrey P Fan**[2], **Zachary B Rodgers**[1], **Erin K Englund**[1], and **Michael C Langham**[1]

[1]Laboratory for Structural, Physiologic and Functional Imaging, Department of Radiology, Perelman School of Medicine, University of Pennsylvania

[2]Lucas Center for Imaging, Department of Radiology, Stanford University

Abstract

The magnetism of hemoglobin – being paramagnetic in its deoxy and diamagnetic in its oxy state – offers unique opportunities to probe oxygen metabolism in blood and tissues. The magnetic susceptibility χ of blood scales linearly with blood oxygen saturation, which can be obtained by measuring the magnetic field ΔB of the intravascular MR signal relative to tissue. In contrast to χ the induced field ΔB is non-local. Therefore, to obtain the intravascular susceptibility $\Delta \chi$ relative to adjoining tissue from the measured ΔB demands solution of an inverse problem. Fortunately, for ellipsoidal structures, to which a straight, cylindrically shaped blood vessel segment conforms, the solution is trivial. The article reviews the principle of MR susceptometry-based blood oximetry. It then discusses applications for quantification of whole-brain oxygen extraction – typically on the basis of a measurement in the superior sagittal sinus – and, in conjunction with total cerebral blood flow, the cerebral metabolic rate of oxygen ($CMRO_2$). By simultaneously measuring flow and venous oxygen saturation (SvO_2) a temporal resolution of a few seconds can be achieved, allowing the study of the response to nonsteady-state challenges such as volitional apnea. Extensions to regional measurements in smaller cerebral veins are also possible, as well as voxelwise quantification of venous blood saturation in cerebral veins accomplished by quantitative susceptibility mapping (QSM) techniques. Applications of susceptometry-based oximetry to studies of metabolic and degenerative disorders of the brain are reviewed. Lastly, the technique is shown to be applicable to other organ systems such as the extremities using SvO_2 as a dynamic tracer to monitor the kinetics of the microvascular response to induced ischemia.

1. Background and Introduction

1.1. Motivation: Quantifying Oxygen Consumption as a Measure of Energy Requirements

All living cells require energy to sustain their function. In mammalian systems, energy is produced by oxidation of nutrients after they are broken down into smaller molecules (usually glucose or fatty acids). In aerobic metabolism the typical end product of this process is carbon dioxide, which is released in the lungs and exhaled while oxygen is inhaled from the air and taken up by hemoglobin in red cells. Knowledge of the metabolic rate of oxygen (MRO_2) provides us with a direct measure of energy consumption. MRO_2 is therefore a key physiologic parameter. In organs such as muscle of the peripheral skeleton or the heart, MRO_2 varies widely as a function of the work-load, ranging from about 1 to 50 ml

O_2/100g/ min for resting and contracting muscle, respectively. In contrast, brain, i.e. cerebral MRO_2 (typically referred to as $CMRO_2$) remains on the order of 3 ml (~130 μmol) O_2/100g /min regardless of the functional demand of different brain activities. Even during light sleep there is only a minor reduction in $CMRO_2$ (1), and only during deep sleep (2) and particularly during anesthesia (3), is energy demand substantially lower.

CMRO_2 can be obtained from a measurement of the arteriovenous oxygen difference, $AV O_2$ = $SaO_2 - SvO_2$, where SaO_2 and SvO_2 are the arterial and venous hemoglobin oxygen saturations, respectively, and blood flow (rate), BF, to or from the organ of interest, expressed in ml blood/100g tissue/min, via Fick's Law, as:

$$CMRO_2 = C_a \cdot AVO_2 \cdot BF \quad [1]$$

where C_a is a constant expressing the blood's oxygen carrying capacity (836μmol O_2/100ml blood at hematocrit of 0.42). There has been much recent interest to quantify $CMRO_2$ via image-based methods. The ability to noninvasively map oxygen utilization by the brain would provide new insight into brain physiology and enable evaluation of pathology-induced disruption of normal brain metabolism in disorders such as Alzheimer's disease, multiple sclerosis and cancer.

Much of prior research on image-based $CMRO_2$ mapping has been conducted by positron emission tomography (PET), achieved by quantifying $H_2{}^{15}O$ after inhaling $^{15}O_2$, and measuring blood flow rate based on injection of $H_2{}^{15}O$ used as a blood flow tracer (4). The method has since been refined and streamlined, and has provided unique information on the brain's response to external stimuli (5). Although PET is widely regarded the gold standard for $CMRO_2$ mapping, it has several limitations. First, it is highly invasive, requiring both arterial and venous punctures, as well as exposure to radiation. The complexity and cost of the protocol, and the need for an on-site cyclotron to produce the ^{15}O tracers, have so far confined PET-based $CMRO_2$ mapping to very few sites possessing these capabilities.

While some work has shown that ^{17}O, the only NMR active nucleus among the three oxygen isotopes, can serve as a tracer analogous to ^{15}O in PET, the high cost of isotopically enriched ^{17}O, and the complexity of the set-up, make it all but impractical in humans (6). In contrast, methods that exploit the paramagnetism of deoxyhemoglobin as a source of contrast in MRI have significantly advanced the field during recent years.

Even though quantification of $CMRO_2$ (and for that matter MRO_2 in general), demands knowledge of both SvO_2 and CBF, obtaining SvO_2 is the far greater problem. MRI-based methods for quantification of SvO_2 can be broadly categorized based on the MR contrast methods employed: T_2 (7,8), T_2^* (BOLD) (9), T_2' (10), and susceptibility-based approaches (11). Most of the former approaches involve complex models relating their respective relaxation rates to blood deoxyhemoglobin concentration. In distinction, susceptibility based methods rely on a simple linear relationship between blood deoxyhemoglobin concentration and blood magnetic susceptibility. Susceptibility-based methods have other distinct advantages, including the possibility of high temporal resolution for application to dynamic

quantification of SvO_2. In keeping with the scope of this Special Issue of the Journal, this article focuses on susceptibility-based methods only.

1.2. Volume Magnetic Susceptibility of Whole Blood

Hemoglobin, ubiquitous in vertebrates, is arguably the most thoroughly studied metalloprotein. It is the fundamental carrier of oxygen, enabling its transport by the blood from the lungs to organs for energy production. A key physical property on which virtually all magnetic resonance methods rely for gaining quantitative insight into oxygen metabolism is hemoglobin's magnetism, first studied systematically by Pauling and Coryell in 1936 (12). In its deoxy state all but two of the six d-electrons of Fe^{2+} in each of the four heme moieties occupy separate orbitals, thereby resulting in an electron spin S=2, making deoxyhemoglobin paramagnetic. In contrast, in the oxy state, the slightly increased ligand field splitting between the two pairs of d-orbitals make spin pairing energetically more favorably, resulting in zero net spin, thus making oxyhemoglobin (HbO_2) diamagnetic.

Thulborn et al. (13) studied the oxygenation dependence of T_2 relaxation of blood and showed the transverse relaxation rate ($1/T_2$) to scale linearly with deoxyhemoglobin (dHb) concentration, and demonstrated the effect to be caused by diffusion of water molecules in the locally inhomogeneous fields set up by the different intra- and extracellular magnetic environments. Further, the authors estimated the volume susceptibility difference between fully deoxygenated and fully oxygenated whole blood ($\Delta\chi$ - $\chi_{do} - \chi_{oxy}$) by measuring the difference in the water NMR resonance frequency between the two states. The measurement was performed on a blood sample in a cylindrical tube oriented parallel to the static field of a 270 MHz spectrometer, yielding a value of 0.2ppm (cgs). A decade later, Weisskoff and Kiihne (14) measured the susceptibility of deoxygenated blood by field mapping with an asymmetric spin-echo EPI sequence, on a similar cylindrical sample positioned perpendicular to the main field (1.5 T). The value reported in this work ($\Delta\chi$= 0.18ppm, cgs) was of the same order as that in (13) and served as a basis for subsequent work (see, for example, (15)). In separate work, Ogawa et al measured the NMR difference frequency Δv of the water resonance at v_o = 360 MHz in a concentric tube arrangement parallel to the static field, with the inner tube containing deoxygenated blood at 35% hematocrit (Hct), and water in the annulus (16). In this arrangement the relative frequency shift is related to the susceptibility difference $\Delta\chi$ as $\Delta v/v_o = (4\pi/3)\Delta\chi$ from which the authors obtained value of 1×10^{-6}. When extrapolated to 100% Hct, this value corresponds to $\Delta x_{do} = 2.86 \times 10^{-7}$, cgs and is in remarkable agreement with values reported much later.

Nevertheless, uncertainties in the value of $\Delta\chi$ remained, which prompted Spees et al to reexamine the problem (17). Invoking Wiedemann's law, the susceptibility of a mixture can be calculated as the volume-fraction weighted mean of its constituents (18). Together with the magnetic moment of Fe^{2+} in deoxyhemoglobin (12), they obtained for the susceptibility difference between completely deoxygenated and completely oxygenated erythrocytes, Δx_{do} = 0.264 ppm (we shall henceforth use the subscript "0" to indicate the susceptibility difference between fully deoxygenated and fully deoxygenated red cells at 100% Hct). The authors corroborated this value experimentally in two different ways, first by measuring the NMR resonance frequency in a cylindrical tube containing blood oxygenated to various

levels, both with the tube parallel and perpendicular to the B_0 field. The frequency difference between these two configurations is given as:

$$\nu_{\parallel}-\nu_{\perp}=2\pi \cdot \Delta\chi_{do} \cdot Hct \cdot (1-Y) \cdot \nu_0 + 2\pi(\chi_{oxy}-\chi_{air}) \quad [2]$$

where ν_0 is the spectrometer frequency and Y the oxygen saturation, the remaining symbols are self-explanatory. From Eq. 2 one recognizes that at a given hematocrit the slope of $\Delta\nu$ versus Hct(1-Y) yields $\Delta\chi$ independent of the susceptibility of air. The value obtained in this manner, 0.27±0.03 ppm, agrees well with their prediction based on the known magnetic moment of Fe^{2+} in deoxyhemoglobin. The second experiment based on SQUID magnetometry yielded Δx_{do} = 0.27±0.02 ppm, again in excellent agreement with the NMR results.

More recently, Jain et al. further corroborated these results, using field mapping techniques (19). *HbO$_2$* saturation was quantified for a range of oxygen saturation levels by field-mapping on freshly drawn human blood from seven donors. The experimental arrangement involved sample tubes of length to diameter ratio ~10 (satisfies the long cylinder approximation), parallel to the main field and immersed in distilled water. The resulting data were compared with results from blood gas analysis. Figure 1 shows field maps for a range of oxygen saturation values along with a plot of MRI-derived *Hct*-weighted susceptibilities measured relative to water. From these images, Δx_{do} was computed as the slope of the linear relation:

$$\frac{\Delta\chi}{Hct}=\Delta\chi_{do}(1-Y)+\Delta\chi_{oxy} \quad [3]$$

Regression analysis yielded (0.273 ± 0.006) and −0.008 ± 0.003 ppm (cgs) respectively, for Δx_{do} and Δx_{oxy}, in excellent agreement with the work by Spees et al (17).

2. Quantitative Imaging Approaches

2.1. Fundamentals of Susceptometry-Based Oximetry

Susceptometry-based methods for quantifying blood oxygen saturation in blood vessels has its foundation in the special behavior of ellipsoidally shaped magnetized objects (see, for instance, Schenck (20)). While for all other irregularly shaped objects numerical methods are needed (21), the induced field inside an ellipsoid is homogeneous and the field outside can be calculated analytically. Of particular interest in this context is the rotational ellipsoid with an aspect ratio (long /short axis)→ ∞ based on the notion that a blood vessel resembles a long cylinder. In this case, the following simple relationship holds between the z-component, ΔB_{int} of the induced field, relative to the field distant from the cylinder:

$$\Delta B_{int}=\frac{\Delta\chi}{2} \left(cos^2\theta-\frac{1}{3} \right) B_0 \quad [4]$$

In Eq. 4 (which includes the Lorentz sphere correction), $\Delta\chi$ is the difference in susceptibility between the two compartments, and θ is the angle of the cylinder axis with respect to the applied field B_0. The relative field outside the vessel is homogeneous as long as its axis is parallel to B_0. More generally, ΔB_{ext} obeys the following relationship (20):

$$\Delta B_{ext}= \left(\tfrac{\Delta\chi}{2} sin^2\theta \cdot \tfrac{a^2}{r^2} \cdot \cos 2\varphi \right) B_0 \quad [5]$$

In Eq. 5, a is the vessel radius, r is the distance perpendicular to the vessel axis, and φ is the azimuthal angle. The geometric parameters in Eqs. 4 and 5 are defined in Figure 2.

The induced field ΔB_{int} inside the vessel can be obtained by measuring the phase difference between the intra- and extravascular signal as long as the inhomogeneity outside the vessel is negligible, i.e. if $\Delta B_{ext} \approx 0$ can be assumed. Eq. 5 suggests that for small angles, i.e. $\theta < 20^0$ ($sin^2 \theta \sim 01$), ΔB_{ext} falls off quickly with a/r, decreasing to <1% five cylinder (i.e. vessel) radii away from the vessel axis. Further, because of the sinusoidal dependence on the azimuthal angle φ, ΔB_{ext} averages to zero within a circular tissue reference region.

The local field offset ΔB is obtained from the phase difference between two successive echoes as:

$$\Delta\varphi(x, y)=\gamma \cdot \Delta B \cdot \Delta TE \quad [6]$$

where $\Delta\psi(x,y)$ is the inter-echo phase difference at pixel location (x,y), and ΔTE is the inter-echo time.

Combining Eqs. 3, 4 and 6 yields for the venous blood oxygen saturation SvO_2:

$$SvO_2=1-\frac{2|\Delta\varphi_{ie}|}{\gamma B_0 \cdot \Delta TE \cdot \Delta\chi_{do} \cdot Hct(\cos^2\theta - 1/3)}+\frac{\Delta\chi_{oxy}}{\Delta\chi_{do}} \quad [7]$$

We note that Eq. 7 assumes that $\Delta B_{ext} \approx 0$. Here, $\Delta\varphi_{ie} = \Delta\varphi_{intra} - \Delta\varphi_{extra}$ represents the intra- to extravascular inter-echo phase difference. Vessel orientation is determined from axial images while hematocrit is obtained from a blood draw.

The initial work toward quantification of whole-brain SvO_2 was conducted in the internal jugular veins (22). However, this location turns out to be difficult in practice due to the large induced fields resulting from the air spaces in the neck. It is for this reason that most subsequent whole-brain susceptometry was performed in the superior sagittal sinus (*SSS*).

2.2. Sources of Systematic Error and Correction Methods

Deviations of Blood Vessel from Cylindrical Geometry—Blood vessels – in
particular veins – rarely conform to the straight cylinder model. They exhibit curvature, branching and tapering, and veins, by virtue of much lower blood pressure, often do not have circular cross section. A case in point is the *SSS*, which has triangular cross-section,

conforming to the small space in the longitudinal fissure immediately adjacent to the skull. Langham et al computed the error in SvO_2 analytically for a long, straight elliptical cylinder (a shape most typically found for the veins of the lower extremities) as a function of eccentricity $\varepsilon = \frac{a}{a+b} - \frac{1}{2}$ where a and b are the long and short axes of the cylinder (23). They found for a vessel tilt angle of 20º and eccentricity $\epsilon = 0.2$ the error did not exceed ±2% SvO_2 from typical nominal values. The problem was also addressed numerically by Li et al (24) using a voxel-based perturbation method (25). They found that at typical SvO_2 levels of 65%, the absolute error in $\%HbO_2$ estimated via a closed-form cylinder approximation was <3 $\%HbO_2$ averaged over three locations in the three veins studied (SSS, jugular and femoral vein) and did not exceed 5% for vessel tilt angles <30º at any one location. Finally, the error was also evaluated experimentally in phantoms containing gadolinium-doped water range of susceptibility values encountered in venous blood (11). The authors found that for a long triangular prism (mimicking the SSS) the mean difference between the susceptibility values did not exceed 2.6% from those measured in circular cross-section tubes, which would correspond to an average absolute difference of 0.8% SvO_2 at hematocrit of 0.42 and SvO_2 of 65%. As shown in (23), the cross-sectional geometry has little or no effect if the vessel tilt angle is small. The data thus suggest the infinite cylinder model to be remarkably accurate for SvO_2 quantification.

Large-Scale Magnetic Field Gradients—Perhaps the main source of error in MR susceptometry is static field inhomogeneity caused by susceptibility mismatch at the interface between the tissue and the surrounding air ($\Delta\chi \sim 9$ ppm). High-pass filtering (see for example, (26)) is commonly implemented to reduce the effect of the static field inhomogeneity characterized by low spatial-frequency modulations on field maps. However, high-pass filtering implemented in k-space *indiscriminately* affects the phase to be quantified in a manner dependent on filter size. Therefore, the high-pass filter cannot separate static or background field inhomogeneity from the field offset relative to the susceptibility difference between intravascular blood and surrounding tissue.

The effects of field inhomogeneity are significantly reduced by fitting the phase difference image $\Delta\varphi(x,y)$ to a second-order polynomial to estimate the macroscopic or low spatial-frequency field variation as:

$$\Delta\varphi(\mathrm{x}, \mathrm{y}) \approx c_o + c_1 x + c_2 y + c_3 xy + c_4 x^2 + c_5 y^2 \quad [8]$$

Here, x and y are coordinates in the 2D image plane, and coefficients c_i are determined through a weighted least-squares fit. The key step before fitting the field inhomogeneity to second-order polynomial of Eq. 8 is weighting the phase difference image by the corresponding magnitude image after masking out the vessels and suppressing the background (27).

The adverse effect of indiscriminate high-pass filtering on the measured hemoglobin saturation levels was investigated in (27). The results demonstrate that the venous saturation measurement is critically dependent on filter size, which is typically determined subjectively to achieve a desired level of uniformity in phase images. Further, after a critical filter size

(n>10) images become visually indistinguishable. It should be noted that the "critical" size is dataset-dependent and the extent to which the images are visually distinguishable depends on the window level.

Figure 3 shows the effect of polynomial background field correction in two subjects for the determination of SvO_2 in the SSS.

2.3. Quantitative Susceptibility Mapping (QSM) for Regional and Voxelwise Oximetry

Mapping OEF along veins—Instead of relying on a vessel model, recent advances in susceptibility imaging allow for SvO_2 to be quantified more generally in veins of arbitrary orientation and geometry by means of quantitative susceptibility mapping (QSM). The method is discussed in greater detail in other articles of this Special Issue of NMR in Biomedicine. In brief, QSM takes a measured local field, ΔB, and aims to recover the underlying susceptibility distribution, $\Delta\chi$, that gives rise to the induced field (28,29). The reconstructed $\Delta\chi$ map reflects the susceptibility effect of deoxyhemoglobin (dHb) in the venous tree. Intravenous susceptibility, and the corresponding oxygen saturation, can then be mapped along all resolved cerebral veins. QSM requires solution of the following inverse problem in Fourier space:

$$\mathscr{F}(\Delta B) = \mathscr{F}(\Delta\chi) \cdot \left(\frac{1}{3} - \frac{k_z^2}{k^2}\right) \quad [9]$$

where $\mathscr{F}$ is the Fourier operator, $D = \frac{1}{3} - \frac{k_z^2}{k^2}$ is the dipole kernel, and k is the magnitude of the k-space vector (30). Unfortunately, this inversion is fraught with difficulties because of the singularities that occur for D near the magic angle (54.7°). Accurate quantification of OEF in veins thus requires careful selection of the QSM algorithm and parameters for narrow vessel structures.

Various QSM algorithms have been used in initial studies to assess venous oxygenation. Haacke et al (31) mapped susceptibility in vessels through use of thresholded k-division, which restricts the minimum value of D to avoid division by zero during QSM reconstruction (32). From this study, the relative susceptibility values in large veins draining deep gray matter corresponding to SvO_2 ranging from 66.1% – 79.3%. During caffeine ingestion, QSM values in veins also showed expected signal increases, corresponding to increased dHb content (i.e. lower SvO_2). Although thresholded k-division successfully removed dipolar field patterns around vessels perpendicular to the main field, streaking artifacts occurred in the QSM image volume that remain to be addressed in future work.

Other QSM studies used regularization to incorporate prior knowledge about the underlying susceptibility, to solve the dipole inversion. Fan et al. measured susceptibility in veins through use of L1-regularization (33), which gives a QSM map that tends to be piecewise constant within anatomical tissue boundaries (34). Figure 4 shows SvO_2 maps superimposed on venograms from healthy volunteers based on L1-regularized QSM maps; mean baseline SvO_2 values from QSM ranged from 61.8 – 66.7% across subjects. This QSM approach also revealed expected increases in SvO_2 in pial veins during breathing of mild levels of CO_2,

which is known to globally increase SvO_2 in the brain (35). Xu et al used a different, non-linear regularization approach (36) to create QSM maps with more sophisticated correction for flow artifacts in veins (37). This work yielded a similar mean SvO_2 of 72.2% ± 4% in cerebral pial veins across subjects.

The above studies suggest QSM as a promising approach to map baseline SvO_2 along the venous tree. While physiologically plausible, some caution should be exercised in comparing the SvO_2 values in these limited studies (Table 1) because the methods used for background field removal and QSM reconstruction differ. For instance, the regularization methods likely smooth and underestimate vessel susceptibility, and are sensitive to the regularization parameters chosen as part of the QSM reconstruction.

Mapping of tissue OEF in response to exogenous challenges—Recent work has investigated the potential of frequency mapping and QSM for obtaining quantitative information on changes in tissue oxygenation in response to functional activation. The recognition that functional *dHb*-dependent effects are more pronounced on MRI phase than magnitude images (38), prompted two groups to use QSM time series to probe tissue oxygenation changes during motor and visual tasks at 7 Tesla (39); and during finger-tapping task at 3 Tesla (40). These functional QSM studies offer a quantitative way to map tissue BOLD changes without geometric dipole contaminations, but focus on functional responses instead of baseline oxygenation. More work is needed to understand the different sensitivity and activation patterns of functional QSM relative to magnitude-based approaches.

To map baseline oxygenation in tissue, Zhang et al proposed a method that requires collection of QSM images and perfusion data in two isometabolic brain states, chosen to be pre- and post caffeine ingestion (41). The caffeine challenge globally alters SvO_2 in the tissue but is assumed not to change oxygen metabolism. The authors created SvO_2 maps at 3 mm isotropic resolution and observed a decrease in SvO_2 from 66.1% ± 10% (before caffeine) to 45.5% ± 13% (after caffeine) across gray matter. While promising, this method to map tissue SvO_2 requires use of a challenge (e.g. caffeine vasoconstriction) and separate perfusion imaging in both brain states, which may be difficult to implement in clinical settings.

Potential sources of error in susceptibility maps—Most of the reported SvO_2 values from QSM (Table 1) are higher than ^{15}O PET measurements ranging from 58% to 64% (42–44). Partial volume artifacts likely lead to underestimation of susceptibility in narrow veins and overestimation of SvO_2 from QSM, especially in pial veins. This consideration naturally restricts the smallest vein diameter that can be used for local SvO_2 measurement, and has motivated careful work on susceptibility measurements in narrow cylinder structures (45,46). Improved spatial resolution (0.4-mm isotropic) achievable at ultra-high field has the potential to expand the method to smaller veins (47). These smaller veins may better indicate local brain function. Recent work further suggests joint use of magnitude and phase images to simultaneously estimate partial volume fraction and SvO_2, so as to minimize partial volume effects in parallel vessels (48).

Residual flow artifacts, especially in large veins, may also contribute to SvO_2 overestimation from QSM maps. These flow artifacts occur due to moving spins in veins through an inhomogeneous magnetic field gradient and persist even in spite of the use of velocity compensation. Xu et al showed that second-order flow artifacts may overestimate baseline SvO_2 at 3 Tesla in pial veins (37). Vessels near the periphery of the brain such as the sagittal sinus are especially challenging for QSM because of background field removal during preprocessing. Current field removal methods (49,50) require delineation of a brain mask and may provide incorrect results at the brain boundary. For this reason, QSM methods often mask out much of the brain periphery such that reliable SvO_2 values are not available in many of the draining sinuses and pial vessels near the cortical surface. Extensions to these methods have been proposed to recover field map information near the brain edges (51).

Additional technical confounds with QSM include variations in SvO_2 due to vessel orientation. The QSM reconstruction theoretically removes angle-dependent effects of the dipole kernel, such that SvO_2 values are consistent across all vessel angles. However, data from veins oriented near the magic angle is more heavily undersampled, such that QSM algorithms often fail to recover the complete susceptibility information for these vessel segments. As a result, while favorably oriented (e.g. parallel) vessels experience minimal SvO_2 bias, vessels tilted near the magic angle exhibit up to 10% SvO_2 underestimation from QSM maps (34). Future technical developments to segment cerebral veins directly from gradient echo scans (52) can help to visualize the vascular anatomy. This structural information could offer new priors to improve modeling and QSM reconstruction and achieve consistent SvO_2 values across vessel orientations.

3. Integration of Susceptometry and CBF Measurement for Whole-Brain $CMRO_2$ Quantification

3.1. Bi-Level Methods

Quantifying $CMRO_2$ requires knowledge of both SvO_2 and blood flow rate (see Eq. 1). In the brain, quantification of global SvO_2 has to be accompanied by a measurement of total cerebral blood flow (*tCBF*). Typically, the latter is measured by phase-contrast MRI of the major arterial conduits – internal carotid and vertebral arteries – which can be assessed via a single axial imaging slice selected distal to the carotid bifurcation. In this manner, a spatial map of blood flow velocity is obtained that, when averaged spatially across the four main feeding arteries, yields total blood flow rate. Since $CMRO_2$ represents the oxygen consumption per minute, normalized to 100 ml of tissue, *CBF* has to be normalized accordingly in mL/min/100g, which requires knowledge of brain mass, easily obtained from a separate 3D T_1-MPRAGE acquisition.

Ideally, both quantities (SvO_2 and *tCBF*) are measured simultaneously, which is complicated by the different measurement locations (i.e. superior sagittal sinus in the head for SvO_2, feeding arteries in the neck for *tCBF*). Jain et al conceived a method to achieve measurement at the *SSS* and neck in an interleaved fashion with a 4-cycle gradient-recalled echo sequence toggling alternately between the two locations (11). In this manner flow rates are obtained in the arteries of the neck and SvO_2 in the *SSS*. The method, subsequently termed *OxFlow*,

achieves a temporal resolution of 30 seconds and has been shown to be able to yield whole-brain $CMRO_2$ both at baseline and during hypercapnia (53) (Figure 5).

A more recent implementation of the *OxFlow*, referred to as fast *OxFlow* (*F-OxFlow*) provided significantly improved temporal resolution (8s versus 30s), achieved with only three instead of the four interleaves, by sampling a dual-echo in one interleave and compacting the pulse sequence (54). While the three-interleave version causes a slight mismatch in the steady state between the phase-contrast sequence interleaves, this did not cause a significant bias in the data in the baseline values of $CMRO_2$, measured in 10 healthy subjects (123±14 versus 124±12 μmol O_2/100g/min). The authors also provided evidence that the method is able to capture the response to a breath-hold stimulus.

3.2. Single-Vessel OxFlow for High-Speed CMRO$_2$ Measurement

To improve the temporal resolution of *CBF* and SvO_2 measurements phase and velocity mapping can be performed at the same site, e.g. at the *SSS*, as shown by Rodgers et al (55). In this manner a temporal resolution of three seconds was achieved via a combination of view-sharing (56) and *SSS* estimation of *tCBF*. However, since the *SSS* drains only about half the brain (essentially the cortex), a prior calibration scan by means of the full bi-level OxFlow sequence is required to obtain the subject's *SSS* blood flow (*SSSBF*) to *tCBF* ratio before starting a time series of measurements in response to a stimulus. The ratio is subsequently used to convert dynamically measured *SSSBF* to *tCBF*. In a related study in 10 subjects a mean *SSSBF:tCBF* ratio of 0.48±0.03 was found (57). The method was applied in a study of the response to volitional apnea (breath-hold) where high temporal resolution is required due to the transient nature of the stimulus. Figure 6 shows parametric images of *CBF* and phase representative of three temporal periods, along with the fractional changes in arteriovenous difference ($AVO_2 = SaO_2 - SvO_2$), *tCBF* and $CMRO_2$. Subject-averaged maximum changes in *tCBF* and AVO_2 were 43.5±9.4% and 32.1±5.7%, respectively, resulting in a small (6.0±3.5%) but statistically significant (p<0.0005) increase in average end-apneic $CMRO_2$. The results suggest apnea – a mixed hypercapnic and hypoxia stimulus -- to be slightly pro-metabolic, with increased $CMRO_2$ to a breath-hold challenge in healthy individuals. This is consistent with previous data showing hypercapnia to be isometabolic (53,58) and hypoxia to be slightly prometabolic (59). Increased $CMRO_2$ during breath-hold may reflect a physiologic mechanism to buffer the brain's energy supply in anticipation of prolonged oxygen supply.

3.3. Regional Approaches for CMRO$_2$ Measurement

Just as *QSM* reconstruction has enabled mapping of oxygenation, regional maps of $CMRO_2$ can, in principle, be created through combination of phase-based SvO_2 quantification with *CBF* mapping by arterial spin labeling MRI (see, for instance, (60)). However, generating parametric images of tissue SvO_2 in absolute physiologic units on the basis of phase mapping has proven difficult.

An alternative approach toward regional $CMRO_2$ quantification is based on intravascular *QSM* yielding SvO_2 (34,37). Here, SvO_2 from gray matter veins are combined with local *CBF* in a region of interest drawn around the spatial location of the vessel (61). Fan et al

reported mean gray matter $CMRO_2$ of 158 ± 18 μmol/100g/min in healthy volunteers with this approach, and observed elevated $CMRO_2$ in the occipital lobe in good agreement with PET data. One limitation with this approach is that the physiological tissue region drained by each vein is not well characterized, especially in cases of pathology. To define the appropriate ASL tissue ROI for a given vein for which SvO_2 is quantified, imaging of the pertinent venous territory would be required, for example by the spin-labeling MRI approach proposed by Wong et al (62). Furthermore, while regional $CMRO_2$ imaging would be useful to monitor local disturbances in oxygen metabolism, these approaches require longer scan time, especially for volumetric QSM. Thus, scan-time considerations limit the temporal resolution of regional relative to global approaches, and motivate faster gradient echo imaging to make the technique clinically practical (63).

4. Clinical Applications of Susceptibility-Based Oximetry to the Brain

4.1. Brain Oxygenation Measurement in the Fetal and Neonatal Brain

Adequate oxygen metabolism is critical to early development of the brain. From the third trimester until several months after birth, the brain energy source shifts from anaerobic glycolysis to more-efficient aerobic metabolism to meet increasing energy demands as brain structures mature. Disruption of oxygen supply to the fetus can lead to hypoxic ischemic injury, and result in postnatal developmental delays and deficits. For this reason, the ability of MRI to noninvasively probe brain oxygenation and predict ischemia at gestational ages earlier than 36 weeks is important (see for instance, (64)). Fetal imaging of oxygenation is challenging due to fetal motion, maternal breathing, and necessarily large field of views that lead to long scan times. Nonetheless, Dai et al used 1.5 T susceptibility-weighted imaging (SWI) to examine 167 veins in fetuses of 42 pregnant women, and were able to identify the veins of Galen and internal cerebral veins on the SWI scans (65). A separate study in five fetuses (mean gestational age of 33.7 weeks) measured SvO_2 in utero from susceptome-try-based oximetry in the SSS; yielding a mean value across fetuses of 66% ± 9% (66).

In neonates, congenital heart disease (CHD) comprises various anatomical abnormalities of the heart that changes cerebral hemodynamics and metabolism. These infants need to undergo reparative surgery within the first few days of life. A recent study by Jain et al measured $tCBF$ and global $CMRO_2$ in 32 neonates with congenital heart disease before surgery (67). This study encountered unique challenges due to the small size of carotid and vertebral arteries in neonates. Therefore, both flow and phase-based SvO_2 were measured in the SSS, taking into account that this vein drains only 45% of total brain blood flow (see also (55), discussed earlier). The authors performed $CMRO_2$ measurements at rest and during hypercapnia to determine whether neurovascular reactivity was affected by disease. While the CO_2 reactivity in these patients remained intact, baseline CBF (9.7 ml/100g/min) and $CMRO_2$ (23μmol O_2/100g/min) were strikingly low. The data suggest that neonates with severe CHD to have brain physiology similar to that of premature infants, and that low baseline $CMRO_2$ could be predictive of eventual white matter damage affecting cognitive function.

4.2. Obstructive Sleep Apnea

Obstructive sleep apnea (*OSA*) is characterized by structural and functional failure of the upper airways to remain patent during sleep, leading to periodic slowing or stopping of breathing. *OSA* is associated with numerous cerebrovascular and neurologic comorbidities, including impaired cognitive function and cerebral lesions characteristic of hypoxic damage. However, work described previously (55) suggests that *CMRO₂* is maintained, or even increased slightly, in the normal apneic response. In recent work, Rodgers et al hypothesized that patients with *OSA* may not have a normal response to apnea, allowing hypoxic brain damage to occur during nocturnal *OSA* events, and potentially leading to further impairment in cerebrovascular autoregulation. To investigate this hypothesis, the authors applied a fast, single-slice *OxFlow* technique described previously to quantify *CMRO₂* during a breath-hold paradigm in 11 patients with *OSA* and 10 subjects examined for sleep disorders but without a diagnosis of *OSA* (68). Interestingly, while patients with *OSA* did not show a statistically significant difference in *CBF* response, they displayed reduced baseline *CMRO₂* and a reduced *CMRO₂* response to the breath-hold challenge. Baseline *CMRO₂* was 117 ± 38 μmol/100g/min in patients with OSA compared to 152 ± 30 μmol/100g/min in the control group of patients without OSA; *CMRO₂* decreased by 10.9 ± 9% in patients during volitional apnea compared to 4.0 ± 6% in controls (68). These findings were interpreted as suggesting impaired vascular regulation and a resulting inability to maintain *CMRO₂* during apnea in *OSA*. While more work is needed to investigate this potential mechanism of hypoxic brain damage in *OSA*, this study shows that *OxFlow* provides fast and robust quantitative *CMRO₂* measurement capable of detecting both baseline and dynamic differences in brain metabolism in patient populations.

4.3. Cerebrovascular-Metabolic Disorders and Injury

Even short-term loss of oxygen supply can have devastating physiological and functional consequences in many cerebrovascular disorders, most strikingly in acute stroke. While *SWI* has been able to visualize hemorrhage and microbleeds in stroke, perhaps the most exciting prospect is to use susceptibility information quantify oxygenation and thus assess tissue viability (69,70). High oxygen extraction fraction ($OEF = (SaO_2 - SvO_2)/SaO_2 \approx AvO_2$) has been shown to identify salvageable tissue (i.e., the penumbra) in the brain and guide therapy for stroke patients.

A review of 43 publications and 1145 patients found that low T_2^* signal in veins near the infarct, indicative of elevated *dHb* content (and thus increased *OEF*), was common in 81% of *SWI* scans from stroke patients (71). The susceptibility-weighted magnitude signal allows assessment of signal intensity and caliber of specific veins; sufficient *SWI* resolution could be even achieved to study pediatric stroke (72). Recent studies have transitioned to quantify *SvO₂* on high-pass filtered phase images. Li et al examined the change in signal phase in 10 veins each from 10 stroke patients at three time points following onset of stroke (< 24 hours, 2–3 weeks, and 2 months) (73). The results suggested that increased *SvO₂* over time corresponded to better patient outcomes during the follow-up period. Another study went further to directly reconstruct susceptibility maps from 3D gradient echo phase scans in stroke patients. In asymmetrically prominent veins, i.e. dilated veins on the ischemic hemisphere, Xia et al found lower *SvO₂* by 16% – 44% relative to the normal-appearing

hemisphere (74). Phase-based oximetry thus has the potential to noninvasively assess *OEF* by MRI and, combined with perfusion studies, may provide valuable information about tissue viability for imaging-based stratification of stroke patients for treatment.

Phase-derived SvO_2 may also provide an earlier biomarker to monitor neurodegenerative diseases, conceivably before the occurrence of structural damage (e.g. lesions and atrophy) in patients. Fan et al applied cylinder-based oximetry to quantify *OEF* in ~10 cortical veins on high-resolution 7 Tesla phase images (0.33 x 0.33 x 1.0mm^3) of patients with various stages of MS (75). Patients showed a 3.4% *OEF* reduction in gray matter relative to age-matched healthy volunteers ($P = 0.0025$) that was not different across brain regions. Furthermore, cortical *OEF* was an independent predictor of patients' cognitive ability in in terms of processing speed, independent of white and gray matter lesions typical of MS tissue damage. Lastly, regional SvO_2 mapping may have potential to follow patients longitudinally during treatment.

Vascular injury is a frequent aspect of traumatic brain injury (TBI), and likely contributes to the pathogenesis of TBI and subsequent chronic disability (76). Recent human investigations in *TBI* patients probed the potential of *SWI* to assess oxygenation-dependent changes in cerebral veins. In 12 patients with mild TBI, one study observed small decreases in venous susceptibility, suggesting increased SvO_2 in the left thalamostriate and right basal vein of Rosenthal ($P = 0.04$) (77). However, these findings did not correlate with symptoms on neuropsychological testing. Using more advanced quantitative *SWI* approaches Liu et al studied 23 TBI patients and reported relative susceptibility values in deep veins and small hemorrhages. They found mean susceptibility of deep veins and hemorrhagic lesions of 435 – 206 ppb and 108 – 56 ppb (SI), respectively (78).

5. MRI Oximetry of the Extremities

5.1. Temporally-resolved SvO$_2$ as a Dynamic Tracer

The oxygen consumption rate of skeletal muscle can increase by as much as 50-fold during heavy exercise relative to the resting state. The primary mechanism to accommodate greater oxygen demand is hyperemia, i.e. a transient increase in blood flow rate, since storage of oxygen in the form of myoglobin is limited. During hyperemia the blood flow in the conduit artery is markedly increased through reduction of microvascular resistance. The resulting increase in shear rate to the endothelium after cuff release leads to vasodilation of the conduit artery, typically induced by nitric oxide release (79).

MR susceptometry-based oximetry offers an opportunity to evaluate vascular dysfunction in the lower extremities by monitoring SvO_2 in the femoral vein in response to a physiological challenge such as cuff-induced ischemia. Vascular dysfunction is well known to occur in peripheral artery disease (PAD) as well as in early, presymptomatic atherosclerosis, for instance, caused by cigarette smoking. Following disruption of the inflow of oxygenated blood via occlusion of a major supplying artery such as the femoral or popliteal artery with a blood pressure cuff, the tissue oxygen store will gradually deplete, and the desaturated capillary blood can serve as an endogenous tracer. Upon restoration of flow via cuff release gradual replacement of the oxygen-depleted blood in the capillary bed can be monitored by

mapping oxygen saturation in the femoral vein. From the time-course of SvO_2 vascular reactivity can be expressed in terms of three parameters (80): *washout time*, *upslope* and *overshoot* (Figure 7). Washout time and upslope provide quantitative information on the washout rate of oxygen-depleted blood from the tissue as well as the rate at which tissue is resaturated. The overshoot may reflect the magnitude of hyperemia since tissue has reduced time to extract O_2, a time consuming process driven by diffusion. Thus, the rise in SvO_2 above baseline is expected in the event of more pronounced hyperemia. Conversely, impaired flow in patients with PAD leads to prolonged O_2 extraction time, thereby contributing to reduced upslope and overshoot. The principle of the method has been described in Sections 2.1 and 2.2, optimized for temporal resolution to accurately map the SvO_2 versus time curve (80). A phase difference image is then computed between two successive echoes of equal polarity (to minimize off-resonance errors). In distinction to applications in the brain the pulse sequence includes spectrally selective fat saturation to reduce contamination from fat near the muscle and first-moment nulling along the slice (i.e. blood flow) direction and flow is temporally resolved via projection velocimetry.

5.2. Dynamic Oximetry in Patients with Peripheral Arterial Disease

One of the most common disorders of the peripheral vasculature is PAD, in which atherosclerosis causes narrowing of the major arteries supplying the lower extremities (iliac, femoral, popliteal and the runoff arteries). The initial diagnosis of patients with PAD is made on the basis of the ankle-brachial index (ABI, ratio of blood pressure at the ankle and radius). A low ABI is a strong indicator of the presence of PAD but a normal ABI does not rule out risk due to relatively high false negative rates (81). Thus, a direct physiological measurement would be desirable for more accurate clinical assessment.

Dynamic oximetry is able of capturing reduced capacity of the peripheral vascular system to respond to a challenge such as cuff-induced ischemia. In a recent study involving three cohorts (Table 2): patients with PAD, older healthy controls (OHC) and young healthy subjects (YH), highly significant differences in oximetric parameters were observed between OHC and PAD. Further, the upslope and overshoot parameters were sensitive to age as shown in Table 2. A subsequent study found that washout time was not only related to PAD disease presence, but was also significantly correlated with patients' ABI as a clinical measure of disease severity (82).

Another recent study applying dynamic oximetry focused on the effect of cigarette smoking in asymptomatic subjects (83). Cigarette smoking is a well-known cause of vascular dysfunction, characterized by a reduction in the bioavailability of nitric oxide (NO), leading to impaired endothelium-dependent vasodilation (84). The study enrolled a total of 169 subjects divided into four groups: young healthy non-smokers (YNS: N = 45, mean age = 30.2 ± 0.7 years, age range: 26–40 years), age-matched young smokers (YS: N = 39, mean age = 32.1 ± 0.7), older healthy non-smokers (ONS: N = 45, mean age = 57.8 ± 0.6 years, age range: 51–65 years), and age-matched older smokers (OS: N = 40, age = 56.3 ± 0.6). All study participants were free of symptomatic CVD as a means to test the method's ability of detecting early, preclinical manifestations of endothelial dysfunction. Figure 8 summarizes the differences in the oximetric parameters between the four cohorts. The results are

consistent with the notion of age- and smoking-related impaired microvascular reactivity. Importantly, for all functional and parameters evaluated the effects of smoking and age were independent of one another.

5.3. Quantification of Skeletal MRO$_2$ in Response to Exercise

Maximal pulmonary oxygen uptake (*VO$_2$max*), defined in terms of the Fick principle as left ventricular (end-diastolic volume – end-systolic volume) × heart rate × arteriovenous oxygen difference, is the gold standard measure of an individual's cardiorespiratory capacity (85). Decreased *VO$_2$max* is a hallmark of heart failure associated with decreased exercise tolerance (86). Isolation of large muscle *VO$_2$* during an exercise paradigm may provide additional insight into the mechanisms that contribute to decreased exercise tolerance in those at risk for or with heart failure. With this goal in mind, Mathewson et al (87) demonstrated feasibility of estimating peak exercise *VO$_2$* and the recovery time constant of VO$_2$ associated with post-exercise (off-kinetics) in healthy males after a period of knee extensor exercise, which targeted the quadriceps femoris muscles. Quantification of *SvO$_2$* and blood flow velocity in proximal superficial femoral vein was performed sequentially with dynamic oximetry and 1D MR velocimetry (88). Each measure took 2.4 s, resulting in effective temporal resolution of 4.8 s. The mean baseline and peak exercise *VO$_2$* was 0.68 and 9.6 ml O$_2$/ 100g/ min, respectively. Lastly, Thompson et al. found statistically significant ($p<0.05$) correlation between quadriceps muscle mass and peak *VO$_2$*.

Concluding Remarks

This review was not meant to be comprehensive, and techniques not directly relying on a susceptibility measurement, including *qBOLD* (10), calibrated BOLD (9) and *T$_2$*-based blood oximetry (e.g. TRUST (8)), have deliberately been omitted, to adhere to the intended scope of this Special Issue of the journal. MRI oximetry exploiting hemoglobin magnetism for assessing oxygen metabolism is still in its infancy. An exception is global *CMRO$_2$*, which can now be measured reliably by means of susceptometry via quantification of venous oxygen saturation in a large draining vein, in conjunction with measurement of cerebral blood flow. The simple inversion procedure to extract intravascular magnetic susceptibility, based on the analytical solution for ellipsoids, is also applicable to smaller veins, but the method suffers from inadequate knowledge of the tissue volume drained. *QSM* has been used with some success for regional mapping of oxygenation in the venous tree and, in at least one instance, to estimate baseline *CMRO$_2$*. Expected advances of current approaches toward voxelwise *CMRO$_2$* mapping techniques would provide additional insight into neurocognitive disorders and facilitate monitoring of the response to therapeutic intervention. Lastly, applications to other organ systems, including skeletal tissues, are emerging.

References

1. Madsen PL, Schmidt JF, Holm S, Vorstrup S, Lassen NA, Wildschiodtz G. Cerebral oxygen metabolism and cerebral blood flow in man during light sleep (stage 2). Brain research. 1991; 557(1–2):217–220. [PubMed: 1747754]

2. Madsen PL, Schmidt JF, Wildschiodtz G, Friberg L, Holm S, Vorstrup S, Lassen NA. Cerebral O2 metabolism and cerebral blood flow in humans during deep and rapid-eye-movement sleep. Journal of applied physiology. 1991; 70(6):2597–2601. [PubMed: 1885454]

3. Renou AM, Vernhiet J, Macrez P, Constant P, Billerey J, Khadaroo MY, Caille JM. Cerebral blood flow and metabolism during etomidate anaesthesia in man. British journal of anaesthesia. 1978; 50(10):1047–1051. [PubMed: 708546]

4. Mintun MA, Raichle ME, Martin WR, Herscovitch P. Brain oxygen utilization measured with O-15 radiotracers and positron emission tomography. J Nucl Med. 1984; 25(2):177–187. [PubMed: 6610032]

5. Raichle ME, Gusnard DA. Appraising the brain's energy budget. Proceedings of the National Academy of Sciences of the United States of America. 2002; 99(16):10237–10239. [PubMed: 12149485]

6. Mellon EA, Beesam RS, Elliott MA, Reddy R. Mapping of cerebral oxidative metabolism with MRI. Proceedings of the National Academy of Sciences of the United States of America. 2010; 107(26):11787–11792. [PubMed: 20547874]

7. Wright GA, Hu BS, Macovski A. Estimating oxygen saturation of blood in vivo with MR imaging at 1.5 T. Journal of Magnetic Resonance Imaging. 1991; 1(3):275–283. [PubMed: 1802140]

8. Xu F, Ge Y, Lu H. Noninvasive quantification of whole-brain cerebral metabolic rate of oxygen (CMRO2) by MRI. Magnetic resonance in medicine. 2009; 62(1):141–148. [PubMed: 19353674]

9. Blockley NP, Griffeth VE, Simon AB, Buxton RB. A review of calibrated blood oxygenation level-dependent (BOLD) methods for the measurement of task-induced changes in brain oxygen metabolism. Nmr Biomed. 2013; 26(8):987–1003. [PubMed: 22945365]

10. Yablonskiy DA, Sukstanskii AL, He X. Blood oxygenation level-dependent (BOLD)-based techniques for the quantification of brain hemodynamic and metabolic properties - theoretical models and experimental approaches. Nmr Biomed. 2013; 26(8):963–986. [PubMed: 22927123]

11. Jain V, Langham MC, Wehrli FW. MRI estimation of global brain oxygen consumption rate. Journal of cerebral blood flow and metabolism : official journal of the International Society of Cerebral Blood Flow and Metabolism. 2010; 30(9):1598–1607.

12. Pauling L, Coryell CD. The Magnetic Properties and Structure of Hemoglobin, Oxyhemoglobin and Carbonmonoxyhemoglobin. Proceedings of the National Academy of Sciences of the United States of America. 1936; 22(4):210–216. [PubMed: 16577697]

13. Thulborn KR, Waterton JC, Matthews PM, Radda GK. Oxygenation dependence of the transverse relaxation time of water protons in whole blood at high field. Biochimica et Biophysica Acta (BBA) - General Subjects. 1982; 714(2):265–270. [PubMed: 6275909]

14. Weisskoff RM, Kiihne S. MRI susceptometry: image-based measurement of absolute susceptibility of MR contrast agents and human blood. Magnetic resonance in medicine. 1992; 24(2):375–383. [PubMed: 1569876]

15. Haacke EM, Lai S, Reichenbach JR, Kuppusamy K, Hoogenraad FG, Takeichi H, Lin W. In vivo measurement of blood oxygen saturation using magnetic resonance imaging: a direct validation of the blood oxygen level-dependent concept in functional brain imaging. Human brain mapping. 1997; 5(5):341–346. [PubMed: 20408238]

16. Ogawa S, Lee T-M. Magnetic resonance imaging of blood vessels at high fields: In vivo and in vitro measurements and image simulation. Magnetic resonance in medicine. 1990; 16(1):9–18. [PubMed: 2255240]

17. Spees WM, Yablonskiy DA, Oswood MC, Ackerman JJ. Water proton MR properties of human blood at 1.5 Tesla: magnetic susceptibility, T(1), T(2), T*(2), and non-Lorentzian signal behavior. Magnetic resonance in medicine. 2001; 45(4):533–542. [PubMed: 11283978]

18. Cerdonio M, Morante S, Vitale S. Magnetic susceptibility of hemoglobins. Methods Enzymol. 1981; 76:354–371. [PubMed: 6276650]

19. Jain V, Abdulmalik O, Propert KJ, Wehrli FW. Investigating the magnetic susceptibility properties of fresh human blood for noninvasive oxygen saturation quantification. Magnetic resonance in medicine. 2012; 68(3):863–867. [PubMed: 22162033]

20. Schenck JF. The role of magnetic susceptibility in magnetic resonance imaging: MRI magnetic compatibility of the first and second kinds. Medical physics. 1996; 23(6):815–850. [PubMed: 8798169]

21. Marques JP, Bowtell R. Application of a fourier-based method for rapid calculation of field inhomogeneity due to spatial variation of magnetic susceptibility. Concept Magn Reson B. 2005; 25B(1):65–78.

22. Fernández-Seara MA, Techawiboonwong A, Detre JA, Wehrli FW. MR susceptometry for measuring global brain oxygen extraction. Magnetic resonance in medicine. 2006; 55(5):967–973. [PubMed: 16598726]

23. Langham MC, Magland JF, Epstein CL, Floyd TF, Wehrli FW. Accuracy and precision of MR blood oximetry based on the long paramagnetic cylinder approximation of large vessels. Magnetic resonance in medicine. 2009; 62(2):333–340. [PubMed: 19526517]

24. Li C, Langham MC, Epstein CL, Magland JF, Wu J, Gee J, Wehrli FW. Accuracy of the cylinder approximation for susceptometric measurement of intravascular oxygen saturation. Magnetic resonance in medicine. 2012; 67(3):808–813. [PubMed: 21858859]

25. Jenkinson M, Wilson JL, Jezzard P. Perturbation method for magnetic field calculations of nonconductive objects. Magnetic resonance in medicine. 2004; 52(3):471–477. [PubMed: 15334564]

26. Wang Y, Yu Y, Li D, Bae KT, Brown JJ, Lin W, Haacke EM. Artery and vein separation using susceptibility-dependent phase in contrast-enhanced MRA. J Magn Reson Imaging. 2000; 12(5): 661–670. [PubMed: 11050635]

27. Langham MC, Magland JF, Floyd TF, Wehrli FW. Retrospective correction for induced magnetic field inhomogeneity in measurements of large-vessel hemoglobin oxygen saturation by MR susceptometry. Magnetic resonance in medicine. 2009; 61(3):626–633. [PubMed: 19107914]

28. Wang Y, Liu T. Quantitative susceptibility mapping (QSM): Decoding MRI data for a tissue magnetic biomarker. Magnetic resonance in medicine. 2014

29. Koch KM, Papademetris X, Rothman DL, de Graaf RA. Rapid calculations of susceptibility-induced magnetostatic field perturbations for in vivo magnetic resonance. Phys Med Biol. 2006; 51(24):6381–6402. [PubMed: 17148824]

30. Salomir, R., de Senneville, BD., Moonen, CT. Concepts Magn Reson. Vol. 19. Wiley Online Library; 2003. A fast calculation method for magnetic field inhomogeneity due to an arbitrary distribution of bulk susceptibility; p. 26-34.

31. Haacke EM, Tang J, Neelavalli J, Cheng YC. Susceptibility mapping as a means to visualize veins and quantify oxygen saturation. J Magn Reson Imaging. 2010; 32(3):663–676. [PubMed: 20815065]

32. Shmueli K, de Zwart JA, van Gelderen P, Li TQ, Dodd SJ, Duyn JH. Magnetic susceptibility mapping of brain tissue in vivo using MRI phase data. Magnetic resonance in medicine. 2009; 62(6):1510–1522. [PubMed: 19859937]

33. Bilgic B, Fan AP, Polimeni JR, Cauley SF, Bianciardi M, Adalsteinsson E, Wald LL, Setsompop K. Fast quantitative susceptibility mapping with L1-regularization and automatic parameter selection. Magnetic resonance in medicine. 2014; 72(5):1444–1459. [PubMed: 24259479]

34. Fan AP, Bilgic B, Gagnon L, Witzel T, Bhat H, Rosen BR, Adalsteinsson E. Quantitative oxygenation venography from MRI phase. Magnetic resonance in medicine. 2014; 72(1):149–159. [PubMed: 24006229]

35. Fan AP, Evans KC, Stout JN, Rosen BR, Adalsteinsson E. Regional quantification of cerebral venous oxygenation from MRI susceptibility during hypercapnia. Neuroimage. 2015; 104:146–155. [PubMed: 25300201]

36. Liu T, Wisnieff C, Lou M, Chen W, Spincemaille P, Wang Y. Nonlinear formulation of the magnetic field to source relationship for robust quantitative susceptibility mapping. Magnetic resonance in medicine. 2013; 69(2):467–476. [PubMed: 22488774]

37. Xu B, Liu T, Spincemaille P, Prince M, Wang Y. Flow compensated quantitative susceptibility mapping for venous oxygenation imaging. Magnetic resonance in medicine. 2014; 72(2):438–445. [PubMed: 24006187]

38. Bianciardi M, van Gelderen P, Duyn JH. Investigation of BOLD fMRI resonance frequency shifts and quantitative susceptibility changes at 7 T. Hum Brain Mapp. 2014; 35(5):2191–2205. [PubMed: 23897623]

39. Balla DZ, Sanchez-Panchuelo RM, Wharton SJ, Hagberg GE, Scheffler K, Francis ST, Bowtell R. Functional quantitative susceptibility mapping (fQSM). Neuroimage. 2014; 100:112–124. [PubMed: 24945672]

40. Chen Z, Calhoun V. Intrinsic functional brain mapping in reconstructed 4D magnetic susceptibility (chi) data space. J Neurosci Methods. 2015; 241:85–93. [PubMed: 25546484]

41. Zhang J, Liu T, Gupta A, Spincemaille P, Nguyen TD, Wang Y. Quantitative mapping of cerebral metabolic rate of oxygen (CMRO) using quantitative susceptibility mapping (QSM). Magnetic resonance in medicine. 2014

42. Ito H, Ibaraki M, Kanno I, Fukuda H, Miura S. Changes in cerebral blood flow and cerebral oxygen metabolism during neural activation measured by positron emission tomography: comparison with blood oxygenation level-dependent contrast measured by functional magnetic resonance imaging. Journal of cerebral blood flow and metabolism : official journal of the International Society of Cerebral Blood Flow and Metabolism. 2005; 25(3):371–377.

43. Ishii K, Sasaki M, Kitagaki H, Sakamoto S, Yamaji S, Maeda K. Regional difference in cerebral blood flow and oxidative metabolism in human cortex. J Nucl Med. 1996; 37(7):1086–1088. [PubMed: 8965174]

44. Ibaraki M, Miura S, Shimosegawa E, Sugawara S, Mizuta T, Ishikawa A, Amano M. Quantification of cerebral blood flow and oxygen metabolism with 3-dimensional PET and 15O: validation by comparison with 2-dimensional PET. J Nucl Med. 2008; 49(1):50–59. [PubMed: 18077532]

45. Hsieh CY, Cheng YC, Neelavalli J, Haacke EM, Stafford RJ. An improved method for susceptibility and radius quantification of cylindrical objects from MRI. Magn Reson Imaging. 2015; 33(4):420–436. [PubMed: 25633922]

46. Hsieh CY, Cheng YN, Xie H, Haacke EM, Neelavalli J. Susceptibility and size quantification of small human veins from an MRI method. Magn Reson Imaging. 2015

47. Deistung A, Schafer A, Schweser F, Biedermann U, Turner R, Reichenbach JR. Toward in vivo histology: a comparison of quantitative susceptibility mapping (QSM) with magnitude-, phase-, and R2*-imaging at ultra-high magnetic field strength. Neuroimage. 2013; 65:299–314. [PubMed: 23036448]

48. McDaniel, P., Fan, AP., Bilgic, B., Stout, JN., Adalsteinsson, E. Improved accuracy in susceptibility-based OEF measurements by mitigation of partial-voume effects via combined magnitude and phase reconstruction. Toronto, Canada: 2015. p. 3330

49. Schweser F, Deistung A, Lehr BW, Reichenbach JR. Quantitative imaging of intrinsic magnetic tissue properties using MRI signal phase: an approach to in vivo brain iron metabolism? Neuroimage. 2011; 54(4):2789–2807. [PubMed: 21040794]

50. Liu T, Khalidov I, de Rochefort L, Spincemaille P, Liu J, Tsiouris AJ, Wang Y. A novel background field removal method for MRI using projection onto dipole fields (PDF). Nmr Biomed. 2011; 24(9):1129–1136. [PubMed: 21387445]

51. Topfer R, Schweser F, Deistung A, Reichenbach JR, Wilman AH. SHARP edges: recovering cortical phase contrast through harmonic extension. Magnetic resonance in medicine. 2015; 73(2): 851–856. [PubMed: 24590869]

52. Bazin, PL., Fan, AP., Mianowska, G., Olbrich, A., Schaefer, A., Villringer, A., Gauthier, CJ. Automated vessel segmentation from quantitative susceptibility maps at 7 Tesla. Toronto, Canada: 2015. p. 2287

53. Jain V, Langham MC, Floyd TF, Jain G, Magland JF, Wehrli FW. Rapid magnetic resonance measurement of global cerebral metabolic rate of oxygen consumption in humans during rest and hypercapnia. Journal of cerebral blood flow and metabolism : official journal of the International Society of Cerebral Blood Flow and Metabolism. 2011; 31(7):1504–1512.

54. Barhoum S, Langham MC, Magland JF, Rodgers ZB, Li C, Rajapakse CS, Wehrli FW. Method for rapid MRI quantification of global cerebral metabolic rate of oxygen. Journal of cerebral blood flow and metabolism : official journal of the International Society of Cerebral Blood Flow and Metabolism. 2015; 35(10):1616–1622.

55. Rodgers ZB, Jain V, Englund EK, Langham MC, Wehrli FW. High temporal resolution MRI quantification of global cerebral metabolic rate of oxygen consumption in response to apneic challenge. Journal of cerebral blood flow and metabolism : official journal of the International Society of Cerebral Blood Flow and Metabolism. 2013; 33(10):1514–1522.

56. Doyle M, Walsh EG, Blackwell GG, Pohost GM. Block regional interpolation scheme for k-space (BRISK): a rapid cardiac imaging technique. Magnetic resonance in medicine. 1995; 33(2):163–170. [PubMed: 7707905]

57. Rodgers ZB, Englund EK, Langham MC, Magland JF, Wehrli FW. Rapid T2- and susceptometry-based CMRO2 quantification with interleaved TRUST (iTRUST). NeuroImage. 2015; 106:441–450. [PubMed: 25449740]

58. Chen JJ, Pike GB. Global cerebral oxidative metabolism during hypercapnia and hypocapnia in humans: implications for BOLD fMRI. Journal of cerebral blood flow and metabolism : official journal of the International Society of Cerebral Blood Flow and Metabolism. 2010; 30(6):1094–1099.

59. Xu F, Liu P, Pascual JM, Xiao G, Lu H. Effect of hypoxia and hyperoxia on cerebral blood flow, blood oxygenation, and oxidative metabolism. Journal of cerebral blood flow and metabolism : official journal of the International Society of Cerebral Blood Flow and Metabolism. 2012; 32(10):1909–1918.

60. Alsop DC, Detre JA, Golay X, Gunther M, Hendrikse J, Hernandez-Garcia L, Lu H, Macintosh BJ, Parkes LM, Smits M, van Osch MJ, Wang DJ, Wong EC, Zaharchuk G. Recommended implementation of arterial spin-labeled perfusion MRI for clinical applications: A consensus of the ISMRM perfusion study group and the European consortium for ASL in dementia. Magnetic resonance in medicine. 2014

61. Fan AP, Benner T, Bolar DS, Rosen BR, Adalsteinsson E. Phase-based regional oxygen metabolism (PROM) using MRI. Magnetic resonance in medicine. 2012; 67(3):669–678. [PubMed: 21713981]

62. Wong, EC., Guo, J. VENTI: Venous Territory Imaging using Remote Sensing. Salt Lake City, UT, USA: 2013. p. 103

63. Bilgic B, Gagoski BA, Cauley SF, Fan AP, Polimeni JR, Grant PE, Wald LL, Setsompop K. Wave-CAIPI for highly accelerated 3D imaging. Magnetic resonance in medicine. 2015; 73(6):2152–2162. [PubMed: 24986223]

64. Liu P, Chalak LF, Lu H. Non-invasive assessment of neonatal brain oxygen metabolism: A review of newly available techniques. Early Hum Dev. 2014; 90(10):695–701. [PubMed: 25028136]

65. Dai Y, Dong S, Zhu M, Wu D, Zhong Y. Visualizing cerebral veins in fetal brain using susceptibility-weighted MRI. Clinical radiology. 2014; 69(10):e392–397. [PubMed: 25060932]

66. Neelavalli J, Jella PK, Krishnamurthy U, Buch S, Haacke EM, Yeo L, Mody S, Katkuri Y, Bahado-Singh R, Hassan SS, Romero R, Thomason ME. Measuring venous blood oxygenation in fetal brain using susceptibility-weighted imaging. J Magn Reson Imaging. 2014; 39(4):998–1006. [PubMed: 24783243]

67. Jain V, Buckley EM, Licht DJ, Lynch JM, Schwab PJ, Naim MY, Lavin NA, Nicolson SC, Montenegro LM, Yodh AG, Wehrli FW. Cerebral oxygen metabolism in neonates with congenital heart disease quantified by MRI and optics. Journal of cerebral blood flow and metabolism : official journal of the International Society of Cerebral Blood Flow and Metabolism. 2014; 34(3):380–388.

68. Rodgers ZB, Leinwand SL, Keenan BT, Kini LG, Schwab RJ, Wehrli FW. Cerebral metabolic rate of oxygen (CMRO2) in obstructvie sleep apnea at rest and in response to breath-hold challenge. JCBFM. 2015 in revision.

69. Hermier M, Nighoghossian N. Contribution of susceptibility-weighted imaging to acute stroke assessment. Stroke. 2004; 35(8):1989–1994. [PubMed: 15192245]

70. Santhosh K, Kesavadas C, Thomas B, Gupta AK, Thamburaj K, Kapilamoorthy TR. Susceptibility weighted imaging: a new tool in magnetic resonance imaging of stroke. Clinical radiology. 2009; 64(1):74–83. [PubMed: 19070701]

88. Thompson RB, McVeigh ER. Real-time volumetric flow measurements with complex-difference MRI. Magnetic resonance in medicine. 2003; 50(6):1248–1255. [PubMed: 14648573]

89. Langham MC, Englund EK, Mohler ER 3rd, Li C, Rodgers ZB, Floyd TF, Wehrli FW. Quantitative CMR markers of impaired vascular reactivity associated with age and peripheral artery disease. J Cardiovasc Magn Reson. 2013; 15:17. [PubMed: 23402422]
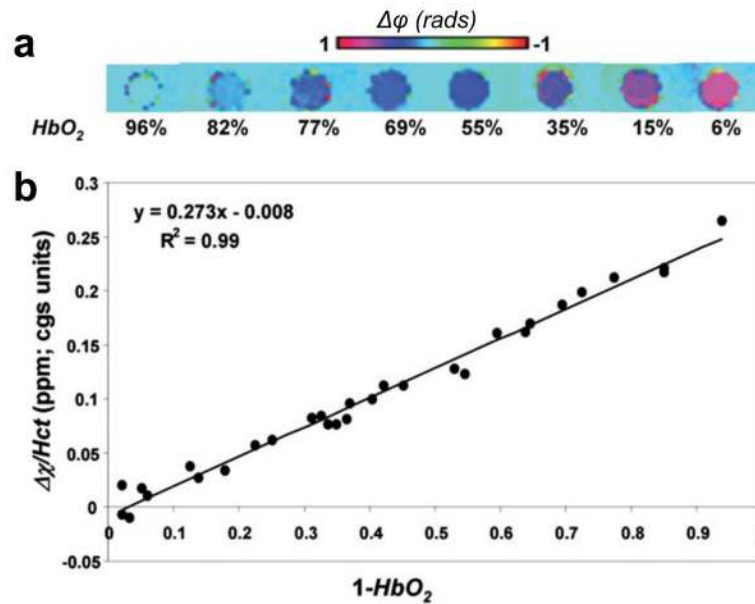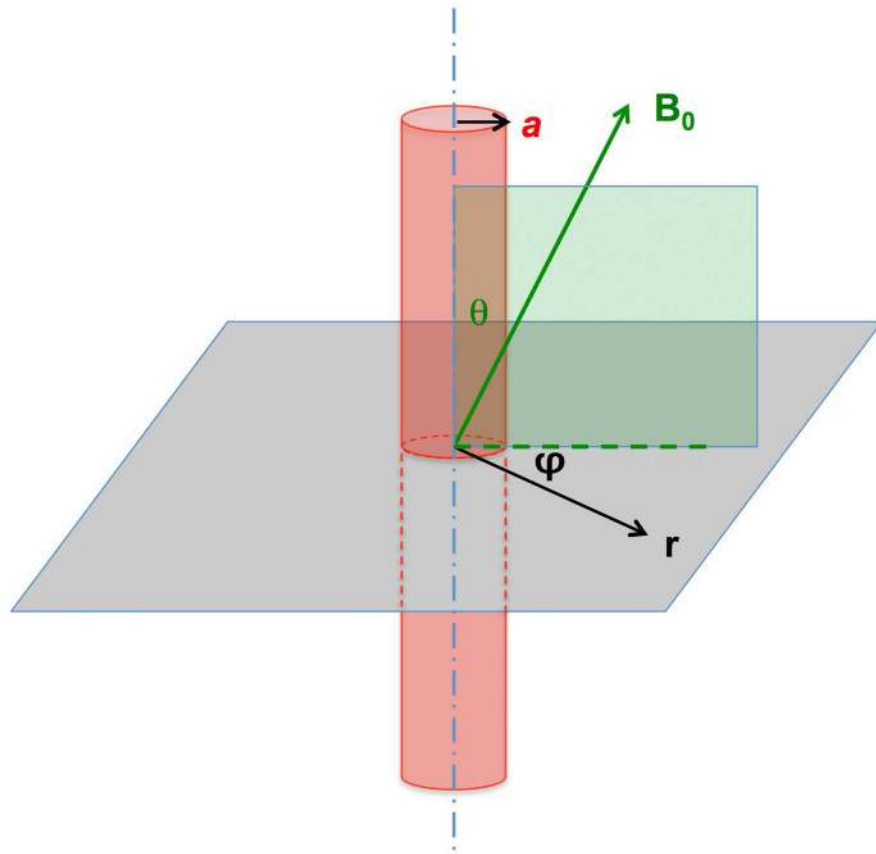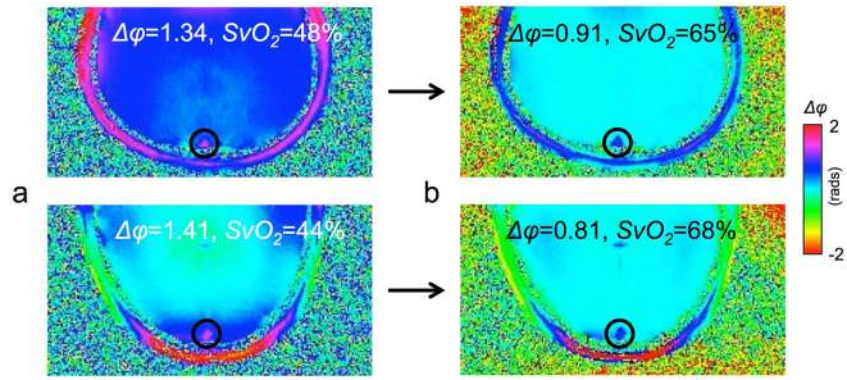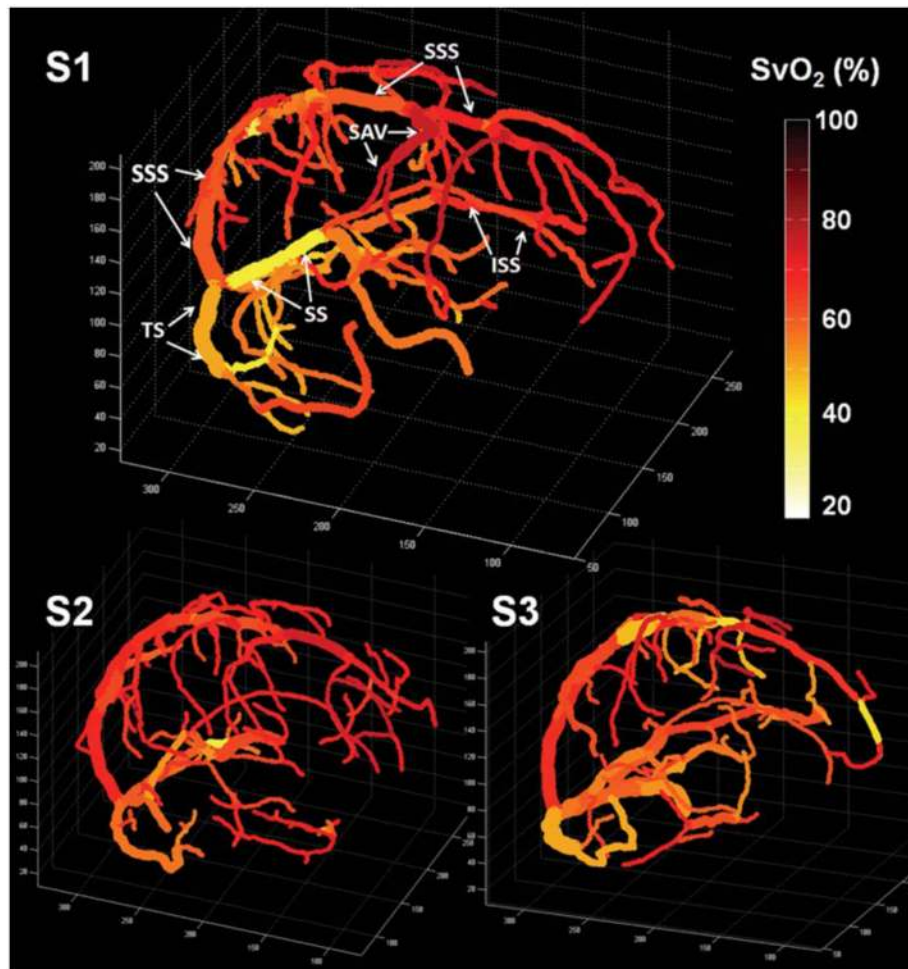
Figure 1.
a) Representative phase difference images of cylindrical sample tubes containing blood oxygenated to various HbO_2 levels, oriented parallel to the B_0 field and immersed in distilled water. b) Susceptibility difference ($\Delta\chi$) between blood and surrounding water normalized to individual Hct level plotted against the level of deoxygenation. The slope of the regression line represents the susceptibility difference between fully oxygenated and deoxygenated blood ($\Delta\chi_{do}$) and intercept $\Delta\chi_{oxy}$ represents the susceptibility difference between fully oxygenated blood and water (from (19), with permission.
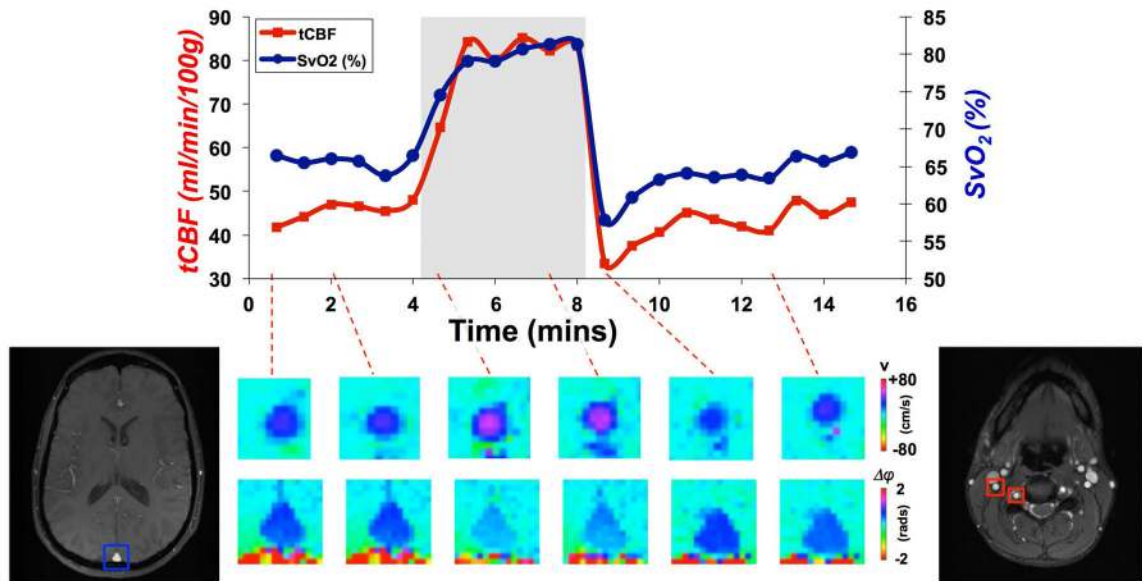
Figure 2.
Relationship between applied field, B$_0$, vessel orientation and angles θ and φ in Eqs. 4 and 5.

Figure 3.
Effect of polynomial fitting on phase maps for two subjects: a) before, b) after fitting. Not only do phase maps become visually more homogeneous but the extracted intra- to extravascular phase difference for the *SSS* yield plausible values for SvO_2 between 60 and 70%.
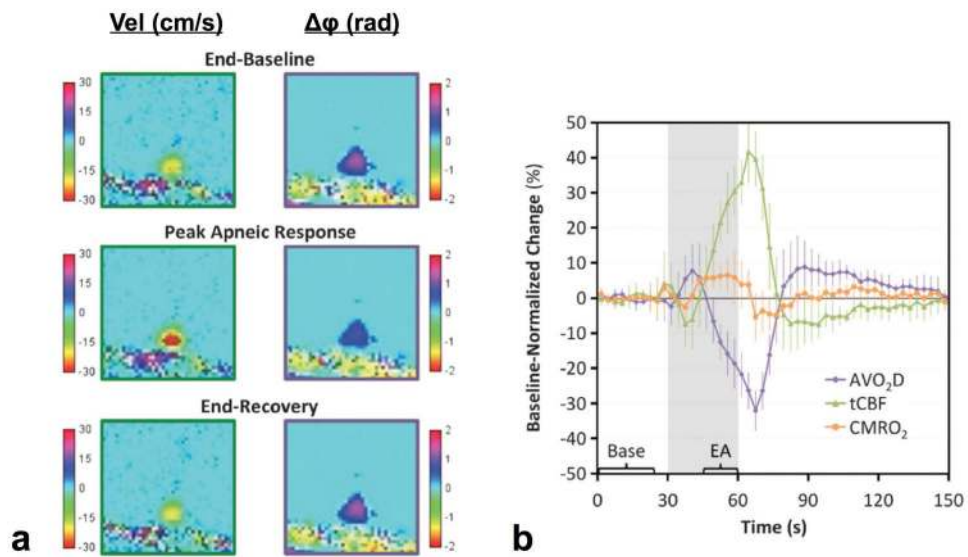
Figure 4.
Quantitative oxygenation venograms display baseline SvO_2 (%) along each vein in three healthy volunteers. In the first subject, major veins in the brain are identified, including the superior sagittal sinus (*SSS*), inferior sagittal sinus (*ISS*), straight sinus (*SS*), transverse sinus (*TS*), and superior anastomic vein (*SAV*). (Reproduced from (34), with permission).
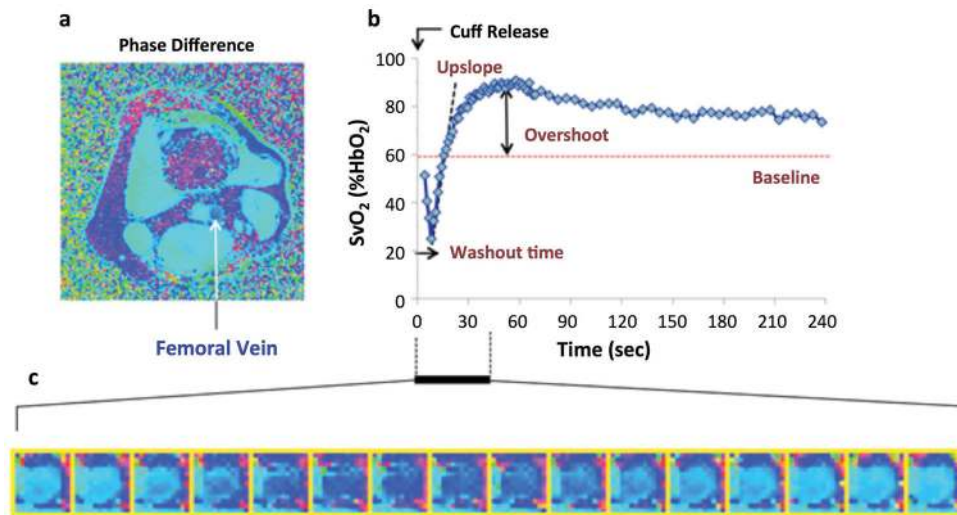
Figure 5.
OxFlow derived time-course at rest and during hypercapnia yielding *tCBF* and *SvO₂* simultaneously. Bottom images display velocity in the right internal carotid artery and phase difference in the *SSS* at select temporal locations (modified, from (53)).
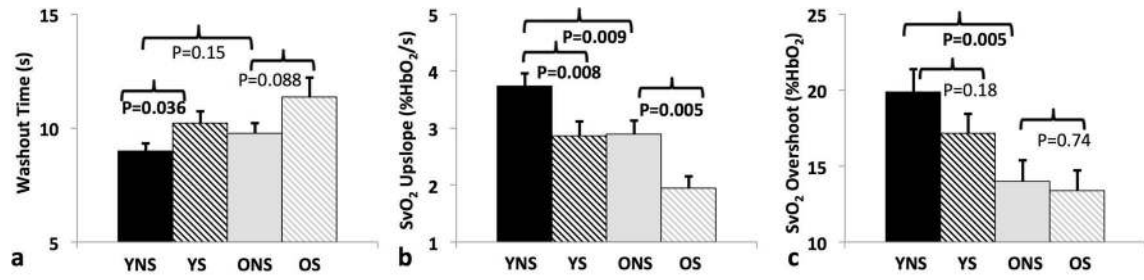
Figure 6.
Effect of volitional apnea on brain vascular-metabolic parameters: a) Expanded parametric maps of flow velocity and phase difference $\Delta\varphi$ (for SvO_2 measurement) obtained with a single-site *OxFlow* sequence acquiring data at the same anatomic site (*SSS*) at 3s temporal resolution, showing enhanced flow and increased SvO_2 (manifested by reduced phase difference) during apnea. b) Fractional changes in parameter values normalized to average baseline. Error bars indicate ±1 SD, gray area the apnea period. Values in time-course plot were averaged across the three repeated blocks of the paradigm. Bracketed sections 'Base' and 'EA' indicate the data used for computing average baseline values and end-apnea values (reproduced from (55), with permission).

Figure 7.
Quantification of reactive hyperemia with dynamic oximetry: **a**) Cross-sectional phase difference image of the thigh, 10 cm below the inferior boundary of the pressure cuff; **b**) post-ischemia femoral vein *SvO₂* time course; **c**) zoomed phase images showing relative phase of venous blood during period indicated. Darker blue represents lower saturation levels. Parameterization of time-course data in panel **b** yields quantitative metrics: washout time, upslope and overshoot (from Langham et al, JCMR 2015, with permission).

Figure 8.
Inter-group comparisons of dynamic oximetric parameters. Data suggest prolonged washout time in smokers (**a**), reduced rate of resaturation (upslope) in both smokers and older subjects (**b**), and similarly, lower overshoot (**c**). Significant p-values (P < 0.05) are highlighted in bold (from reference (83), with permission).

Table 1

Comparison of quantitative susceptibility mapping (*QSM*) studies to map oxygenation.

Study	QSM technique	Veins analyzed	SvO$_2$ values (%)
Haacke et al. (31)	Thresholded k-division	Large veins (8mm – 16mm diameter), e.g. vein of Galen and thalamostriate veins	66.1 – 79.4 (calculated)
Fan et al. (34)	Regularization with L1-penalty	Large sinuses e.g. sagittal sinus, transverse sinus, straight sinus	47.7 – 67.6
		Pial veins e.g. superior anastomic vein	70.2 – 75.3
Xu et al. (37)	Nonlinear dipole inversion	Pial veins	72.2 ± 4 (mean)
Zhang et al. (41)	Regularization with L1-penalty	Tissue voxels	66.1 ± 10 (mean gray matter)

Author Manuscript

Author Manuscript

Author Manuscript

Author Manuscript

Table 2

Average (standard error) of parameters of dynamic oximetry (89).

Groups	N	ABI	Age (years)	Washout (s)	Upslope (%HbO$_2$/s)	Overshoot (%HbO$_2$)
OHC	43	1.12 (0.09)	61 (7.6)	16.9 (1.1)	1.3 (0.08) [*]	14 (1.2) [*]
PAD	38	0.69 (0.15)	64.6 (7.7)	28.6 (1.2) [**]	0.60 (0.1) [**]	8 (1.4) [**]
YH	19	1.1 (0.12)	34.3 (7.5)	15 (1.7)	1.88 (0.13)	19 (1.9)

*and** correspond to statistically significant mean difference between OHC and YH, and between OHC and PAD, respectively.